

An Integrated Computational Model of the Bone Microenvironment in Bone-Metastatic Prostate Cancer

Arturo Araujo¹, Leah M. Cook², Conor C. Lynch², and David Basanta¹

Abstract

Bone metastasis will impact most men with advanced prostate cancer. The vicious cycle of bone degradation and formation driven by metastatic prostate cells in bone yields factors that drive cancer growth. Mechanistic insights into this vicious cycle have suggested new therapeutic opportunities, but complex temporal and cellular interactions in the bone microenvironment make drug development challenging. We have integrated biologic and computational approaches to generate a hybrid cellular automata model of normal bone matrix homeostasis and the prostate cancer-bone microenvironment. The model accurately reproduces the basic multicellular unit bone coupling process, such that introduction of a single prostate cancer cell yields a vicious cycle similar in cellular composition and pathophysiology to models of prostate-to-bone metastasis. Notably, the model revealed distinct phases of osteolytic and osteogenic activity, a critical role for mesenchymal stromal cells in osteogenesis, and temporal changes in cellular composition. To evaluate the robustness of the model, we assessed the effect of established bisphosphonate and anti-RANKL therapies on bone metastases. At approximately 100% efficacy, bisphosphonates inhibited cancer progression while, in contrast with clinical observations in humans, anti-RANKL therapy fully eradicated metastases. Reducing anti-RANKL yielded clinically similar results, suggesting that better targeting or dosing could improve patient survival. Our work establishes a computational model that can be tailored for rapid assessment of experimental therapies and delivery of precision medicine to patients with prostate cancer with bone metastases. *Cancer Res*; 74(9); 2391–401. ©2014 AACR.

Major Findings

- The hybrid cellular automata model recapitulates the key aspects of the physiology of the basic multicellular unit as well as the "vicious cycle" of prostate to bone metastases.
- Progression of osteogenic prostate to bone metastases is critical on osteoclast activity and mesenchymal stromal cells.
- The computational model also illustrates the temporal and phasic nature of the metastases.
- The application of clinically used bisphosphonates and anti-RANKL therapies to the computational model illustrates the power of the approach in predicting the efficacy of current and putative therapies.

Authors' Affiliations: Departments of ¹Integrated Mathematical Oncology and ²Tumor Biology, H. Lee Moffitt Cancer Center and Research Institute, Tampa, Florida

Note: Supplementary data for this article are available at Cancer Research Online (<http://cancerres.aacrjournals.org/>).

A. Araujo and L.M. Cook share first authorship for this article.

C.C. Lynch and D. Basanta share senior authorship for this article.

Corresponding Authors: Arturo Araujo, H. Lee Moffitt Cancer Center, 12902 Magnolia Drive, Moffitt Stabile Research Building (SRB 4), Tampa, FL 33612. Phone: 813-817-2575; Fax: 813-745-6497; E-mail: arturo@cancerevo.org; and Conor C. Lynch, E-mail: conor.lynch@moffitt.org

doi: 10.1158/0008-5472.CAN-13-2652

©2014 American Association for Cancer Research.

Introduction

Prostate cancer frequently metastasizes to bone with approximately 90% of the men displaying evidence of skeletal lesions upon autopsy (1). Despite medical advances, prostate to bone metastases remain incurable with treatments being mainly palliative (2). Advances in our knowledge of the molecular mechanisms underlying the disease should provide therapeutic opportunities to improve overall survival rates but on a more microenvironmental scale, predicting how putative therapies will impact multiple cellular responses remains a challenge. However, integrating key biologic findings with the power of computational modeling offers a unique opportunity to assess the impact of putative therapies on the progression of prostate cancer.

Understanding the normal basic multicellular unit (BMU) bone remodeling process is critical for the generation of a robust computational model (3). The initiation of the BMU by local or systemic signals results in retraction of osteoblasts from the bone surface and the formation of a canopy. Local mesenchymal stromal cells (MSC) generate RANKL-expressing osteoblast precursors that subsequently facilitate osteoclast recruitment, maturation, and bone resorption. Degradation of the bone results in the release of sequestered growth factors such as TGF- β that in turn serve to control the extent of bone degradation and osteoblast expansion. After osteoclast apoptosis, osteoblasts rebuild the bone with a portion terminally differentiating into osteocytes and the remainder reconstituting the bone lining, ready for the next remodeling cycle.

Quick Guide to Assumptions and Equations

For our hybrid cellular automata model, we consider six different cell types, including five residents of the BMU: osteoblasts, osteoclasts, precursor osteoblasts (pOB), precursor osteoclasts (pOC), MSCs, as well as prostate tumor cells, capable of recruiting MSCs and producing TGF- β (Table 1). Next, we considered the interactions between the key cell types (Fig. 1A) and the microenvironmental factors that control those interactions, which were defined as follows.

Bone

Bone is one of the richest reservoirs of TGF- β in the human body (700 pg/mg of bone tissue; ref. 10). We have modeled bone explicitly as static cells that, when resorbed, disappear from the domain and release bone-derived factors (BDF) and TGF- β .

MSCs, pOBs, and osteoblasts

Bone-generating osteoblasts (pOBs) are derived from MSCs (11). MSCs undergo asymmetrical division and pOBs proliferate in response to TGF- β , ultimately differentiating into bone matrix-producing osteoblasts, a process mediated by factors such as BMP-2 (12). In our model, pOBs express RANKL, migrate toward and expand clonally in response to TGF- β , and finally differentiate into osteoblasts after 14 days. As adult osteoblasts, the modeled cells seek TGF- β and bone. If in contact with bone, they lay down bone matrix with an active lifespan of 75 days (Fig. 1B).

pOCs and osteoclasts

pOCs are derived from myeloid precursors and, in response to RANKL, undergo cellular fusion to generate mature osteoclasts (13). Osteoclasts resorb the bone matrix, leading to the release of BDFs and TGF- β (5, 14). We have explicitly modeled these processes. pOCs are recruited by RANKL from the vasculature and have a lifespan of 2 days. Once on the bone surface, they will fuse together, provided that the local levels of RANKL are high, whereas those of TGF- β are low. A minimum of three pOCs (usually 5 or more) can fuse to form an osteoclast. Osteoclasts have a lifespan of 14 days, in which their singular function is to resorb bone thereby releasing TGF- β and BDFs (Fig. 1C). On the basis of the amount of TGF- β present in bone, we have calculated that a single osteoclast measuring 100 μm in diameter will resorb approximately 10 μm^3 of bone per day. Given the density of bone as 1,500 mg/kg, we estimate that an osteoclast can resorb 1.17×10^{-3} mg/day. With the concentration of TGF- β in bone being 5 ng/mg, we calculated that a mature osteoclast can generate up to 0.00558 ng of TGF- β per day.

Prostate cancer

On the basis of our empirical as well as published data, we engineered the prostate cancer cells to express TGF- β ligands and receptors. Importantly, the level of prostate cancer TGF- β (5×10^{-12} pg/day) is approximately 1,000-fold less than that generated by bone resorbing osteoclasts (5×10^{-9} pg/day). This ensures the reliance of the prostate metastases on TGF- β released from the bone. In the computational model, we have described the TGF- β -producing prostate cancer metastases as agents chemoattracted to the BMU, with an ability to recruit MSCs, based on our empirical studies (Fig. 2). Prostate cancer replication potential is proportional to the availability of BDFs and, if not bathed with these essential factors, prostate cancer cells will die within 14 days (Fig. 1D). The prostate cancer metastases are the only ones that can destroy the canopy of the BMU as they grow (Fig. 3B). We have considered that prostate cancer promotes osteoblast differentiation, a phenomenon that is not noted in lytic lesions (14).

The microenvironment

TGF- β , RANKL, and BDFs are generated by the behaviors and interactions amongst the cellular components and are characterized by partial differential equations that are subsequently discretized and applied to a grid. TGF- β is produced by bone destruction ($\alpha_\beta B_{ij}$) and cancer cells ($\alpha_c C_{ij}$) in proportion to the local TGF- β concentration, with natural decay of the ligand ($\sigma_\beta T_\beta$), ensuring the density never exceeds a saturation level, m_0 . TGF- β has pleiotropic effects on osteoblasts, osteoclasts, and metastatic prostate cancer cells. Low concentrations of TGF- β stimulate osteoclastogenesis, but high concentrations inhibit the process, illustrating the biphasic effects of this growth factor even on the same cell type (15, 16). Our group and others have shown that TGF- β supports tumor survival and growth by activating TGF- β receptors (T β R) on the tumor cell surface (17–19). TGF- β is governed by the following differential equation:

$$\frac{\partial T_\beta(x, y, t)}{\partial t} = \nabla(D_\beta(m_0 - M)\nabla T_\beta) + \alpha_\beta B_{ij} + \alpha_c C_{ij} - \sigma_\beta T_\beta$$

RANKL R_L is produced by pOCs, $\alpha_L O_{ij}$, in proportion to the local RANKL concentration, with natural decay of the ligand, $\sigma_L R_L$, ensuring the density never exceeds the saturation level n_0 . The concentration of RANKL is determined by:

$$\frac{\partial R_L(x, y, t)}{\partial t} = \nabla(D_L(n_0 - N)\nabla R_L) + \alpha_L O_{i,j} - \sigma_L R_L$$

Factors F_B are released by bone destruction, $\alpha_B B_{i,j}$, in proportion to the local factor concentration, with natural decay of the factors, $\sigma_B F_B$, ensuring the density never exceeds the saturation level p_0 . As such, the dynamics of the bone-related factors are calculated through:

$$\frac{\partial F_B(x, y, t)}{\partial t} = \nabla(D_B(p_0 - P)\nabla F_B) + \alpha_B B_{i,j} - \sigma_B F_B$$

Periodic boundary conditions were considered only for the left and right sides of the microenvironment, whereas no-flux boundaries were imposed on the top and bottom of the two dimensional grid.

In the metastatic prostate cancer-bone microenvironment, prostate cancer cells perturb the balance of the BMU to generate a "vicious cycle" via the expression of factors such as RANKL thereby inducing excessive bone resorption (4). The release of sequestered growth factors from the bone matrix such as TGF- β in turn stimulates the survival and growth of the metastatic prostate cancer cells. Of note, prostate to bone metastases are also characterized by areas of extensive bone

formation/osteogenesis, a phenomenon that is mediated by factors such as, endothelins and bone morphogenetic proteins, BMP-2 and BMP-4 (5).

To date, the majority of our knowledge of the mechanisms driving prostate cancer progression has been garnered by focusing on the role of individual cancer/host-derived molecules. However, this molecular reductionist approach often does not take into account the multiple cellular effects of

Table 1. Empirical and published data used to parameterize the computational model

Parameter	Value	Normalized value	Reference
Osteoblast diameter	15 μm	1 px	(34)
Osteoclast diameter	50–100 μm	3–5 px	(35)
Osteoclast migration speed	100 $\mu\text{m}/\text{h}$	1 px/ts	(36)
	5 nm/s but can vary between 30 and 248 mm/h.		(37)
			(38)
Osteoblast migration speed	10 $\mu\text{m}/\text{h}$	1/6 px/ts	(36)
	0.1470 \pm 0.02 mm/d		(39)
Cell-cycle time	24 h	240 ts	Estimated
TGF- β diffusion rate	750 $\mu\text{m}^2/\text{min}$	0.01 px/ts	(40)
	2×10^{-9} cm^2/s		(8)
	DPP-10 $\mu\text{m}/2$		(41)
TGF β half-life	2 min	0.5 ts	(42)
	2–3 min. Presence of LAP can extend half-life to 100 min in plasma.		(43)
TGF- β quantity released by OCL/d	0.00558 ng/d	1 MaxTGF- β /ts	Estimated
TGF- β quantity released by tumor cell/d	0.005 pg/d	0.0001 MaxTGF- β /ts	Estimated
Rate of bone degradation	10 $\mu\text{m}/\text{d}$	1/240 px/ts	(44)
	43–1,225 $\mu\text{m}^3/\text{h}$ for \sim 2 wk		(45)
Volume of a resorption pit	78,539 $\mu\text{m}^3 = 7.58 \times 10^{-14}$ m^3	70 px	Assumed from the diameter of an osteoclast and the amount of bone resorbed over a 24-hour period.
Bone formation	0.656 $\mu\text{m}/\text{d}$ but up to 0.24 mm/y	1/850 px/ts	(45)
	1 $\mu\text{m}/\text{d}$		(46)
BMU size	2×0.5 mm^2	200 \times 50 px	Estimated

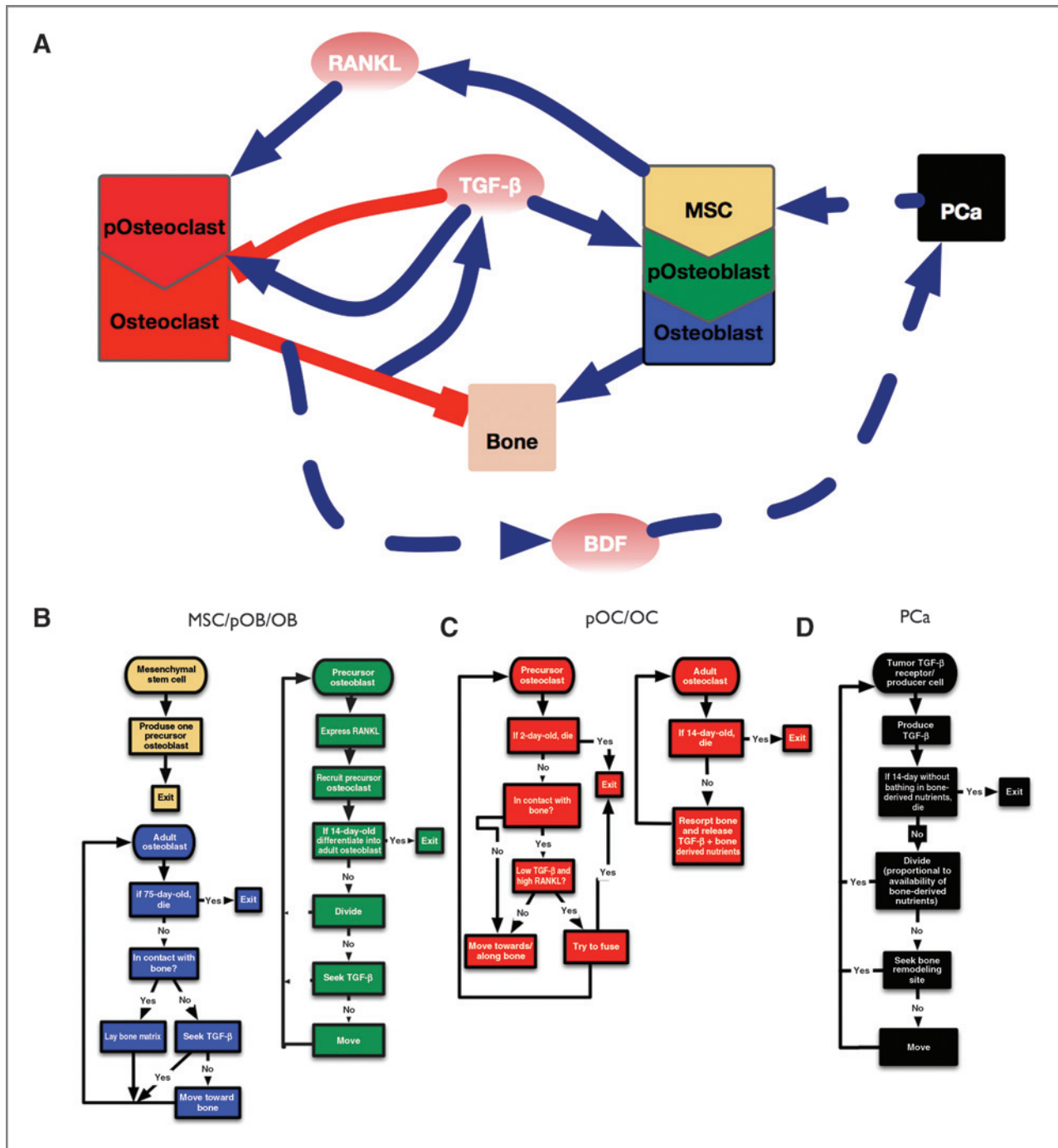
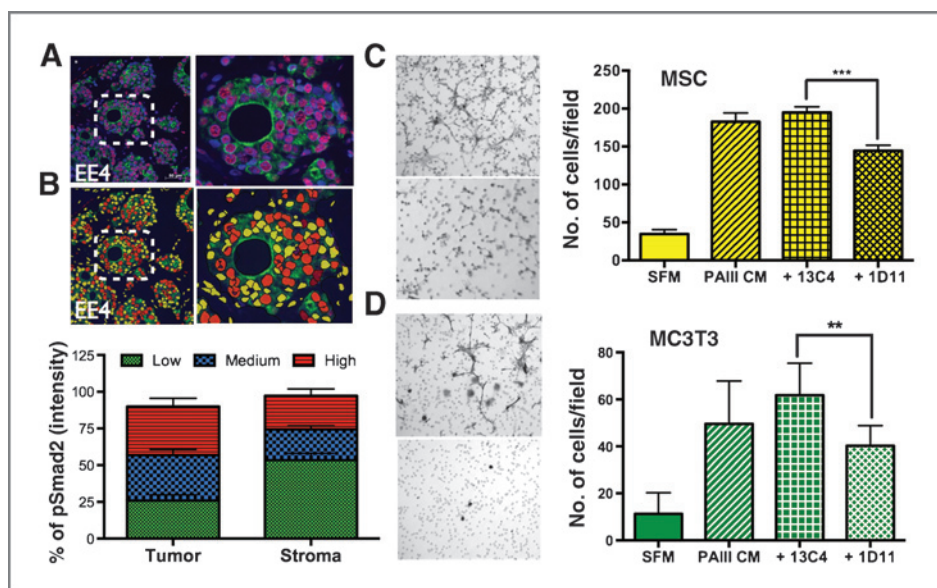


Figure 1. Developing a model of the prostate tumor bone microenvironment. A, interaction diagram showing the positive (blue) and negative (red) interactions between cell types (boxes) and factors such as TGF- β , RANKL, and BDFs. B–D, flowchart describing the sequence of steps followed by osteogenic cells (B), osteolytic cells (C), and prostate cancer cells (D) in the mathematical model. PCa, prostate cancer.

molecular mechanisms being investigated. Mathematical and computational models are a powerful means with which to study complex *in vivo* interactions. Numerous advances using this approach have identified roles for tumor heterogeneity in cancer progression and evolution, accurately predicting glioma progression and response to disease and, describing the cellular dynamics of bone remodeling (6). To

understand the simultaneous and multiple interactions occurring over time in the metastatic prostate cancer bone microenvironment, we have generated a hybrid cellular automaton (HCA)-based integrated computational model. Using this approach, we tested the model's response to therapies currently used in the clinic to treat prostate to bone metastases (7–9). We posit that computational models

Figure 2. TGF- β expression in human prostate to bone metastases. A, patient samples ($N = 9$) were stained for pSMAD2 (red), pan-cytokeratin (green) with nuclear contrast (DAPI). Dashed inset is magnified in panel on right. B, the intensity of pSMAD2 staining in patient samples was assessed using Definiens Tissue Studio software. C and D, TGF- β significantly enhances the migration of MSCs and MC3T3 osteoblast precursors. Representative low power objective ($\times 20$) filters illustrating MSC (C) and MC3T3 (D) migration to prostate cancer conditioned media (PAIII CM) in the presence of a TGF- β blocking antibody (1D11) or IgG control (13C4). Serum-free media (SFM) was used as a baseline control for migration. Asterisks denotes statistical significance ($P < 0.05$).



will be a powerful means with which to test the efficacy of available or putative therapies for the treatment of prostate to bone metastases.

Materials and Methods

Mathematical model

Parameters for the HCA model were derived from empirical and published data (Table 1; ref. 9). The model is composed of a grid (200×50 points) representing $2 \times 0.5 \text{ mm}^2$ of the bone microenvironment. A major advantage of the HCA is in its intimate interconnection with experimental data, where the model and the experiments inform each other. This increases the accuracy of the model abstractions and connectivity of the basic elements, which yields reliable and biologically relevant emergent behaviors. To model the normal sequence of the BMU program, we have focused on understanding the role and behavior of the key regulators of the BMU dynamics. The principal cellular players, bone, MSCs, precursor osteoblasts (pOB), osteoblasts, precursor osteoclasts (pOC), and osteoclasts, have been explicitly modelled as agents in a grid following specific rule sets in a physical microenvironment (see Quick guide to assumptions and equations). Collectively, these components find a natural homeostatic balance that recapitulate the dynamics of bone remodeling, a homeostasis that can be perturbed via the introduction of metastatic prostate cancer cells.

Immunofluorescence and quantitation

Human prostate to bone metastases samples ($5 \mu\text{m}$), provided by Dr. Robert Vessella (University of Washington, Seattle, WA), were rehydrated and blocked before the addition of phospho-specific anti-Smad2 (1:200 dilution; Millipore) and pan anti-cytokeratin (1:200 dilution; Sigma) and appropriate immunoglobulin G (IgG) controls. Tissue sections were incubated overnight at 4°C . Subsequently, species-specific secondary AlexaFluor 568 and AlexaFluor

488-conjugated antibodies (1: 1000 dilution for one hour at room temperature; Invitrogen) were added for imaging by microscopy. For semiquantitative analysis, regional images were segmented on the basis of the intensity of staining using Definiens Tissue Studio (TS).

Migration

Osteoblast (MC3T3) and MSC migration was assessed using a modified Boyden Chamber assay. Cells (5×10^5) were seeded in the upper chamber and their migration to TGF- β rich PAIII conditioned media in the presence of a TGF- β inhibitor (1D11; Genzyme) or isotype control (13C4) at a concentration of $5 \mu\text{g}/\text{mL}$ was measured over a 5-hour period at 37°C . Migrated cells were stained with hematoxylin and air dried. The number of migrated cells was counted in three random $\times 20$ fields for each condition. All experiments were performed in triplicate.

Intratibial Prostate Model of osteogenesis, histology, and TRAcP staining

All animal experiments were done with University of South Florida (Tampa, FL) Institutional Animal Care and Use Committee approval (CCL; #R3886). PAIII luciferase expressing cells were injected (1×10^5 in $10 \mu\text{L}$ volume) into the tibia of anesthetized immunocompromised mice (recombinase activating gene-2 null; RAG-2 $^{-/-}$; ref. 20). Tumor growth was imaged using bioluminescence imaging and quantitated with IVIS Living Image software. After 2 weeks, tumor-bearing tibias were excised, soft tissue removed and processed for histology and histomorphometry as we have previously described (19, 21).

For cell culture and statistical methods, please see Supplementary Materials and Methods.

Results

Key for the generation of the BMU was the incorporation of major cellular players namely the prostate cancer metastases,

MSCs, pOBs, osteoblasts, pOCs, and osteoclasts. Furthermore, based on the literature, RANKL, TGF β , and BDFs were considered main mediators driving the cellular interactions (14). Although RANKL has been well characterized in the context of prostate to bone metastases, few studies have explored the role of TGF- β signaling in this setting. Therefore, we initially examined the activity of TGF- β signaling in prostate to bone metastases in human specimens. Using phosphorylated SMAD2 (pSMAD2) as a readout for TGF- β receptor activity, our results indicated that TGF- β signaling is active in human prostate to bone metastases (Fig. 2A). Quantitative analysis revealed that in the human specimens, TGF- β signaling was highest in the prostate cancer cells but we also observed strong staining in stromal cells, including osteoblasts (Fig. 2B). We also examined the effects of TGF- β on the proliferation and migration of the cellular components of the vicious cycle including prostate cancer cells, osteoclast precursors, and osteoblast precursors, including MSCs. Of note, we observed that TGF- β significantly impacted the migration of MSCs and the osteoblast precursor cell line, MC3T3-E1, suggesting a role of the growth factor in the recruitment of cells that could impact prostate cancer-induced osteogenesis (Fig. 2C and D).

On the basis of these empirical data and the literature, we parameterized a HCA computational model of the homeostatic BMU (Fig. 3A and Supplementary Fig. S1 and Movie 1). On the basis of multiple simulations ($N = 25$) of the computational model, we observed little variation in each population cell number. In some instances ($N = 2$), the BMU failed to initiate, in part, due to spatial and cytokine gradient differences between the different simulations (data not shown) but, we

expect that persistent remodeling initiation stimuli would eventually lead to the formation of the BMU *in vivo*. We also observed that in a subset of BMU simulations ($N = 2$), simultaneous osteoclast fusion resulted in two sites of resorption. However, the generation of BDFs by the osteoclasts sufficiently increased osteoblast numbers and returned the BMU to baseline (data not shown). Importantly, the typical interactions between the different elements of the computational model result in a homeostatic BMU. It is important to note that each of the cells behave as autonomous agents and possess the inherent ability to respond to the surrounding environment independently.

Next, we introduced a single metastatic prostate cancer cell expressing TGF- β ligand and receptors into the BMU. Interestingly, we observed that in many of the simulations ($N = 18$ of 25), the metastases failed to generate a lesion. We anticipate that the introduction of prostate cancer emboli would significantly enhance the "take rate." This "take rate" result emphasizes the stochastic nature of the model and reflects the *in vivo* reality where not every metastatic cancer cell that successfully invades a BMU would result in a viable lesion. In the simulations where lesions were initiated ($N = 7$ of 25), we observed that after 10 days, the presence of the prostate cancer cells resulted in the integrity of the canopy being compromised and a resultant increase in osteoclast recruitment and maturation (Fig. 3B). Over time, the prostate cancer cells expanded, resulting in MSC infiltration and osteoblast-mediated bone formation ultimately recapitulating the "vicious cycle" paradigm (Fig. 3B and Supplementary Fig. S2 and Movie 2).

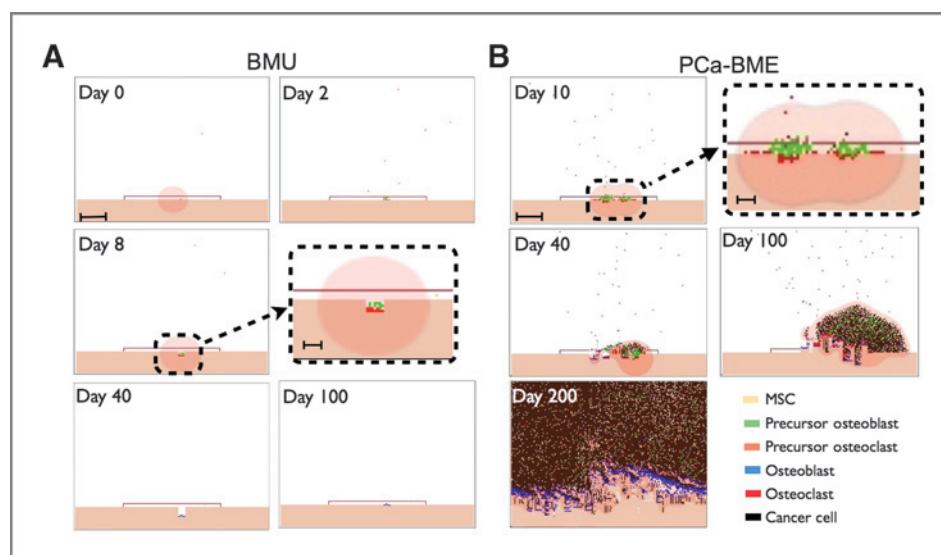


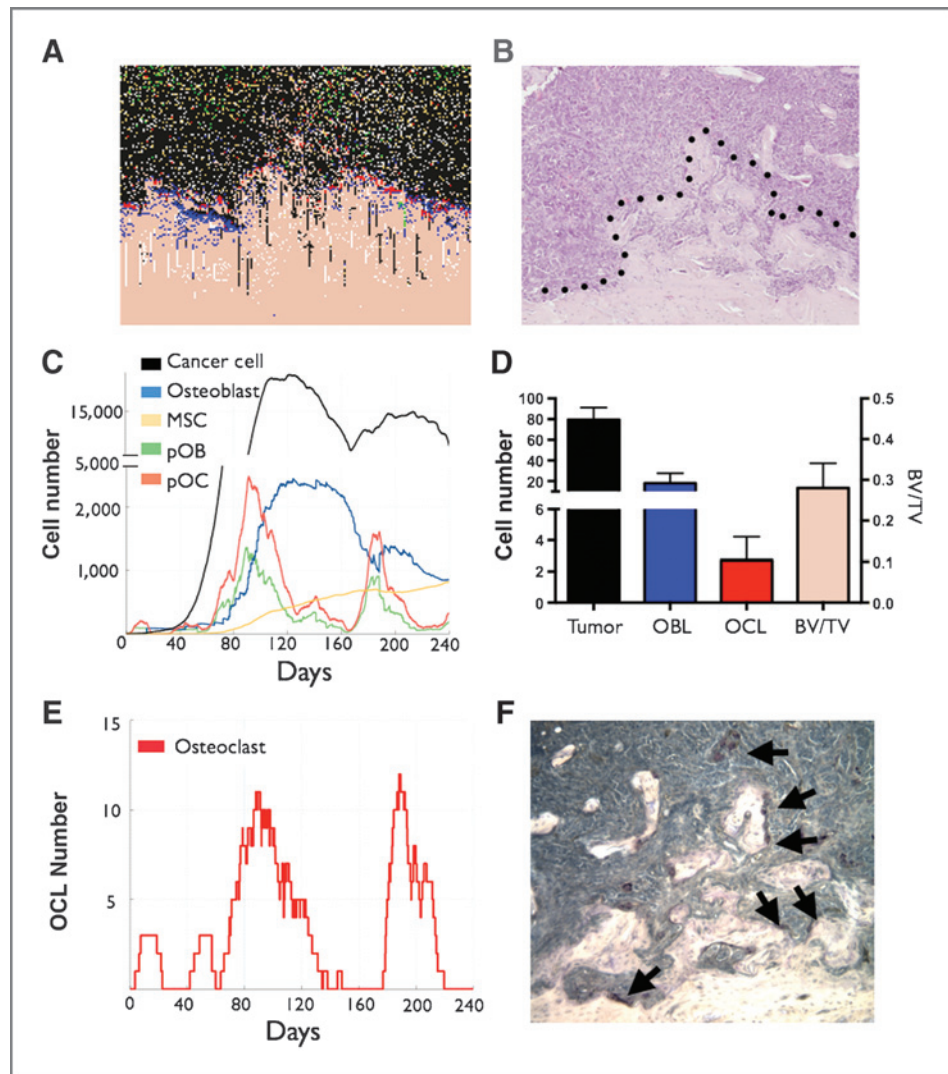
Figure 3. Simulation runs from the BMU model of the bone modeling unit (BMU) and the metastatic prostate cancer bone microenvironment (prostate cancer-BME). A, canopy formation in response to local/systemic stimuli (day 0). Initial osteoid degradation by retracting osteoblasts can result in the release of TGF- β that stimulates pOB expansion subsequent to asymmetric division by MSCs. Scale bar, 250 μ m. pOBs recruit pOCs in a RANKL-dependent manner (day 2). As they fuse, the pOCs become fully differentiated osteoclasts that start resorbing bone. Inset illustrates bone resorption in the BMU. Scale bar, 100 μ m. Upon osteoclast apoptosis, pOBs differentiate into adult osteoblasts and begin the apposition phase (day 40). Osteoblasts rebuild bone over the course of 3 months and undergo terminal differentiation into osteocytes during the process (day 100). B, the introduction of a TGF- β ligand and receptor expressing metastatic prostate cancer cell perturbs BMU homeostasis (day 0). Inset highlights tumor–bone interaction. Scale bars, 250 and 100 μ m, respectively. The BMU canopy is compromised at day 40 and uncontrolled bone turnover results in the enhanced recruitment of MSCs and pOCs that establishes a vicious cycle (day 100–200).

Analysis of the computational prostate cancer-bone micro-environment at day 240 revealed striking histologic similarities to an *in vivo* model of the osteogenic/osteolytic prostate to bone metastasis environment (Fig. 4A and B). We noted that the number of prostate cancer cells varied amongst simulations ($8,625 \pm 4,580$; $N = 5$) but in general, the growth rate predicted by the computational model was comparable with the growth rate of the prostate cancer cells *in vivo* (Supplementary Fig. S3). We also noted similar proportions of stromal cell populations at the computational and biologic study endpoints (Fig. 4C and D). In the computational model, distinct phases of cell activity were observed. For example, the numbers of adult osteoblasts increased over time but notable plateaus before increases in cell number existed (Fig. 4C). These plateaus in adult osteoblasts corresponded with dips in the pOB and pOC precursor population. MSC numbers, however, gradually increased over time and in general, paralleled increases in cancer cell number. In fact, the model predicts that MSCs are crucial for the progression of the metastases because relaxing the probability of recruitment greatly impacts the growth of

the metastases (Supplementary Fig. S4). Furthermore, we observed that osteoclasts were critical for cancer progression in the model with numbers changing over time from zero to 12 (Fig. 4E). Although the *in vivo* model output has a similar number of osteoclasts per field (Fig. 4D and F) at the study endpoint, the phasic nature of osteoclast involvement is not apparent.

To test the applicability of the model in treating prostate to bone metastases, we applied two standard-of-care treatments, namely, a bisphosphonate and an anti-RANKL inhibitor, that induce osteoclast apoptosis during resorption and inhibit osteoclastogenesis, respectively. To mimic the clinical scenario, we applied the bisphosphonate at a time where metastases had established (day 80), although it should be noted that therapies could be applied at any juncture to the model (Fig. 5A and B and D; $N = 5$ simulations per group). During bisphosphonate treatment, osteoclasts still formed but typically died within 24 hours of initiating bone resorption (Fig. 5B, bottom). However, residual bone resorption during bisphosphonate therapy was

Figure 4. Computational and biologic model output comparisons of the prostate cancer-bone microenvironment. A and B, the computational output (A) of the prostate cancer-bone microenvironment is similar to that of an *in vivo* prostate cancer to bone metastasis model (B). Dashed line in B represents the tumor-pathologic bone interface. C, temporal changes in cell population in the computational model. D, analysis of cell populations (prostate cancer cells, bone rimming cuboidal osteoblasts, and TRAcP-positive osteoclasts) and bone volume in biologic model endpoint. E and F, computational model outputs reveal the fluctuation of osteoclast numbers over time (E), numbers that correlate with the numbers of TRAcP osteoclasts (arrows) in similar sized fields *in vivo* (F).



Downloaded from <http://cancerres.aacrjournals.org/cancerres/article-pdf/74/9/2391/12717204/2391.pdf> by guest on 24 April 2024

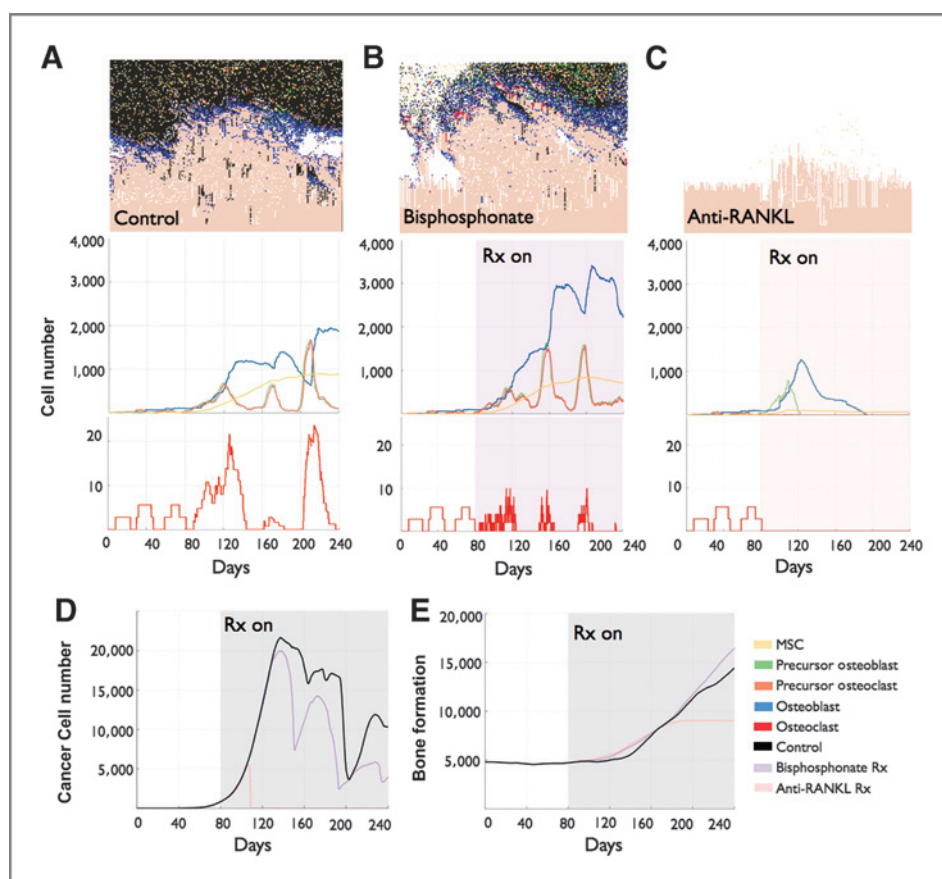


Figure 5. Application of therapies to the computational model of the metastatic prostate cancer bone microenvironment. A–C, the impact of standard-of-care therapies on the host microenvironment cell numbers in prostate to bone metastases was assessed in simulations where no therapy was applied (control; A), bisphosphonates at a dosing of 4 mg/5 mL i.v. (bisphosphonate; B) or RANKL targeted therapy (Anti-RANKL; C) at a dose of 120 mg/1.7 mL i.v. was applied at approximately 80 days postmetastasis (Rx On). D and E, the impact of placebo control and standard-of-care therapies on tumor volume (D) and bone volume (E) over time.

sufficient to sustain the metastases with the number of cancer cells on average at the final time point being $7,138 \pm 2,343$ ($n = 5$) compared with nontreated control of $8,624 \pm 4,580$ ($n = 5$; $P > 0.05$). Interestingly, the application of an anti-RANKL inhibitor halted cancer growth with no cancer cells detectable after 20 days of administration (Fig. 5C and D; $P < 0.05$). These data suggest that treatment with anti-RANKL inhibitors should be curative in the clinical setting. However, in clinical trials with anti-RANKL inhibitors such as Xgeva, there is a slight but not significant increase in survival of patients on the therapy compared with bisphosphonates (2). In our simulations, we found that reducing the efficacy of the anti-RANKL inhibitor from 100% to 40% resulted in an output of cancer cells ($3,157 \pm 3,037$; $N = 5$) that was comparable with that of the bisphosphonate-treated group ($7,138 \pm 2,343$ cancer cells; $N = 5$; Fig. 5B and Supplementary Fig. S5). These data suggest that improved efficacy of anti-RANKL delivery into the prostate cancer bone microenvironment could be curative.

Discussion

In the current study, we have generated a faithful computational model of the BMU. It is important to note that the homeostatic behavior is not hardcoded but emerges from the interactions between the different primary cell types of the bone in response to TGF- β , RANKL, and BDFs. Furthermore, informed by experimental evidence, the introduction of a

simulated TGF- β ligand and receptor expressing prostate cancer cell into the BMU resulted in a vicious cycle that yielded mixed osteogenic/osteolytic lesions over clinically relevant periods of time. Key findings arising from the computational model include: (i) the ability to assess temporal changes in cellular populations and dissect complex dynamics that are difficult to determine *in vivo*, (ii) the phasic osteolytic/osteogenic nature of the metastases, (iii) the application of clinically used therapies such as bisphosphonates and anti-RANKL therapies illustrate the usefulness of the model in predicting the efficacy of targeted inhibitors, and (iv) the impact of inhibitors at varying doses on the progression of prostate to bone metastases.

In our study, we selected the BMU as the primary target for metastatic prostate cancer cells in which to establish and grow. This is logical because reports have shown that high rates of bone turnover correlate with poorer prognoses for patients with prostate cancer and that the metastases can utilize many of the bioavailable factors present in the remodeling environment (22–24). On the basis of this rationale, we introduced a single metastatic prostate cancer cell into the BMU that over time recapitulated the vicious cycle paradigm. The "histologic" output of the computational model at the endpoint was remarkably similar both in morphology and in cellular population proportion to an *in vivo* model used by our group to study mixed prostate to bone metastases. In contrast, however, the computational model illustrates that the cellular

population in the prostate cancer-bone microenvironment is dynamic and changes occur both exponentially (tumor growth) and in phases (osteoclast, osteoblasts). For example, our model illustrates that osteoclast numbers rarely exceed a total of 20 out of approximately 2×10^4 cells per computational field of view (Fig. 4C and E). Reports have shown that high levels of TGF- β can hinder osteoclastogenesis therefore, limiting the number of osteoclasts that can form in the tumor-bone microenvironment even in the presence of RANKL-producing osteoblast precursors (25). In fact, our results show that osteoclast-mediated bone resorption is critical for the induction of the osteogenic metastases, an observation that supports the use of anti-RANKL therapies in men with osteogenic prostate to bone metastases.

In a number of model iterations, we observed that the recruitment of MSCs to the prostate cancer-bone microenvironment was essential for the generation of osteoblast precursors and the development of osteogenic lesions. Our *in vitro* data also show that TGF- β contributes to MSCs and osteoblast precursor migration therefore, providing a means through which these cell types can be recruited to areas of prostate to bone metastases and contribute to their progression (Fig. 2). Although the role of MSCs in the prostate cancer-bone microenvironment has not been explicitly explored thus far, our model predicts an important role for this cell type in tumor growth. It is important to note that we did not consider the trans-differentiation of prostate cancer cells into osteoblasts, but "osteomimicry" is a distinct possibility that could also be integrated into future iterations of the model (26).

The ability to dissect changes in cellular composition in the computational model provides key insights into how the cancer cells, MSCs, osteoblast precursors, osteoblasts, osteoclast precursors, and osteoclasts are interacting with each other over a clinically relevant period of more than 200 days. *In vivo* models are typically analyzed at endpoint or at predetermined time steps to assess cancer growth and changes in the microenvironment in control and test groups. For example, the MDA-MB-231 progression in bone is often measured at weekly time points (27). The computational model generated in this study clearly illustrates that a number of the host microenvironment components, notably the mature osteoclasts and osteoblasts, undergo phases of activity and rest (Figs. 3 and 4). This level of resolution is not available in biologic models but demonstrates that the time points or endpoints chosen for *in vivo* models are a "snapshot" that may not be truly reflective of what has, or is about to happen in the tumor-bone microenvironment. Knowledge of the dynamic changes occurring over time in the computational cancer bone-microenvironment could lead to a better understanding of when to apply inhibitors or what happens to the cell populations over time once inhibitors have been applied.

Bisphosphonates and more recently anti-RANKL therapies are used as treatment strategies to protect patients with prostate to bone metastases from skeletal-related events (SRE). Studies have shown that bisphosphonates can extend the average time to SRE for patients, and anti-RANKL-based therapies are significantly better than bisphosphonates in extending that time to first SRE (2, 28). However, neither

treatment increases overall survival. We applied these inhibitors to our computational model. Assuming an efficacy of 100%, application of a bisphosphonate after a period in which the metastasis is actively growing (day 80) demonstrated an impact on osteoclast activity and on tumor growth. This time point was chosen based on the prostate metastases being established and actively growing but therapeutics could be applied at any juncture, a useful feature to study the response of multiple bone metastases at various stages of progression. Subsequent to the application of bisphosphonates to the model at day 80, we observed that osteoclasts still formed and that the residual production of TGF- β and BDFs was sufficient to sustain tumor growth, albeit to a lesser extent compared with the nontreatment control arm (Fig. 5). Significantly, we also assumed that the dosing of bisphosphonates was at 100% efficacy over the course of the therapy, but, in reality, there are most likely changes in concentrations. Gradients in therapy concentration can be accounted for and pharmacokinetics can be explicitly simulated in the computational model and it will be interesting to determine the impact of dosing gradients on the behavior of the cell populations over time in the computational microenvironment.

Application of an anti-RANKL inhibitor, again at a presumed efficacy of 100%, significantly impacted the prostate tumor-bone microenvironment by preventing osteoclast formation, and subsequently, tumor growth. The model therefore, predicts that anti-RANKL inhibitors should be curative in the clinical setting. However, the clinical reality is that anti-RANKL inhibitors do not significantly extend overall survival in men with metastatic prostate cancer (2). Interestingly, reducing the efficiency of the anti-RANKL therapy to 40% closely mimics that of the bisphosphonate treatment and suggests that increasing doses or better targeting of the anti-RANKL inhibitors to the bone could enhance the efficacy of the drug provided that there are no or minimal increases in noted side effects such as osteonecrosis of the jaw or cataract formation (Supplementary Fig. S3). Clinically, the dosage and frequency of administration of anti-RANKL therapy such as Xgeva are based on trials that demonstrated the optimal balance of efficacy, as determined by a more than 70% decrease in urine N-terminal collagen fragments (NTX), and tolerability was 120 mg subcutaneously delivered every 4 weeks (29). It is possible that higher doses may prove more efficient in significantly enhancing overall survival in patients with prostate to bone metastases as suggested by the computational model but this increase in dose may be outweighed by increased risks of side effects. A major advantage of the computational model is the application of combination or putative therapies to study cellular behavior in the prostate bone-microenvironment over time. For example, our results highlight the role of active TGF- β signaling in the cancer and host cells of human prostate to bone metastases and in the migration of MSCs and osteoblasts (Fig. 2). This observation is in keeping with other studies and underscores the key role TGF- β signaling plays in the bone microenvironment in regards to promoting the progression of prostate to bone metastases. The computational model could therefore easily test the efficacy of TGF- β inhibitors applied to the prostate cancer-bone

microenvironment and predictions used to inform preclinical and ultimately clinical trials.

There are a number of caveats to the computational model described herein. Quantitative predictions from computational models are typically dependent on the information used to parameterize it. The key values used to parameterize the computational model presented in this paper are based on TGF- β and RANKL. The flexibility of the model ensures that ranges in the concentration and balance of other factors and cells that can impact the BMU in the normal and disease setting can be easily integrated. Enhancing these qualities will improve the accuracy of the generated predictions, but our existing model is already quite robust to changes in the parameterization (Supplementary Fig. S4). Although our model is relatively sophisticated, simpler less computationally intensive mathematical models have a number of advantages in that they are easier to understand and analyze. Furthermore, having fewer parameters, they are amenable to the fitting of existing experimental data using techniques such as approximate Bayesian computation (ABC). Fitting extant experimental data to mathematical models has been used successfully to drive a model to closely represent a set of observations in cases such as imatinib response in patients with leukemia (30). These approaches can also provide exact results when sufficient summaries are used (31). Simpler mathematical models are usually preferable, especially when values for biologic parameters are largely unknown (32, 33). In this case, a more complex model was necessary to capture the bone homeostasis emerging from the interactions between MSCs, osteoclasts, osteoblasts, pOCs, and pOBs. The existence of reliable empirical data made it possible to properly parameterize such model. This has allowed us to elucidate the mechanisms involved in the vicious cycle of prostate to bone metastases. One drawback of more complex computational models is that they are computationally intensive and therefore, limiting the ability to perform large numbers of simulations that statistically can explore the robustness of each of the chosen parameters. However, in multiple simulations ($N = 25$), we have ensured that the plausible plasticity of these parameters fall within the currently accepted biologic empirical values. As such, we have focused on investigating changes on the parameters that may vary experimentally; especially molecules such as RANKL and TGF- β that are difficult to measure *in vivo* that have yielded interesting insights (Fig. 5 and Supplementary Materials and Methods). Follow-up experiments will use increased numbers

of simulations to enhance statistical analysis and use new biologic parameters being empirically determined to improve the accuracy of the model predictions.

In conclusion, using empirical and published data, we have generated a hybrid discreet model of the BMU and shown that the introduction of single active metastatic prostate cancer cell into the BMU is sufficient to generate osteogenic lesions that are similar in pathophysiology to those in an animal model of the disease. Furthermore, the application of existing clinical therapies to the computational model underscores the value of this new approach for testing the impact of combining available therapies or putative targeted therapies for the treatment of prostate to bone metastases. Clinically, the versatility of the equations used to build the computational model ensures that it can be quickly individualized and be a powerful tool for the delivery of precision medicine to better treat and cure men with prostate to bone metastases.

Disclosure of Potential Conflicts of Interest

No potential conflicts of interest were disclosed.

Authors' Contributions

Conception and design: A. Araujo, L. Cook, C.C. Lynch, D. Basanta
Development of methodology: A. Araujo, L. Cook, C.C. Lynch, D. Basanta
Acquisition of data (provided animals, acquired and managed patients, provided facilities, etc.): L. Cook
Analysis and interpretation of data (e.g., statistical analysis, biostatistics, computational analysis): A. Araujo, L. Cook, C.C. Lynch, D. Basanta
Writing, review, and/or revision of the manuscript: A. Araujo, L. Cook, C.C. Lynch, D. Basanta
Administrative, technical, or material support (i.e., reporting or organizing data, constructing databases): A. Araujo, D. Basanta
Study supervision: A. Araujo, L. Cook, C.C. Lynch, D. Basanta

Acknowledgments

The authors thank Scott Lonning at Genzyme for the ID11 inhibitor and Lizzie Atomi Pamen for her technical support.

Grant Support

This work was supported by an NCI U01 (U01CA151924-01A1; D. Basanta), the Department of Defense Hypothesis Development Award (W81XWH-12-1-0016; C.C. Lynch and D. Basanta), the National Cancer Institute (RO1CA143094; C.C. Lynch), and the American Cancer Society Post-Doctoral Fellowship (PF-13-175-01-CSM; L.M. Cook). This work was also supported, in part, by the Moffitt Analytical Microscopy Core facility at the Moffitt Cancer Center.

The costs of publication of this article were defrayed in part by the payment of page charges. This article must therefore be hereby marked *advertisement* in accordance with 18 U.S.C. Section 1734 solely to indicate this fact.

Received September 18, 2013; revised March 4, 2014; accepted March 4, 2014; published online May 1, 2014.

References

- Keller ET, Brown J. Prostate cancer bone metastases promote both osteolytic and osteoblastic activity. *J Cell Biochem* 2004;91:718–29.
- Brown JE, Coleman RE. Denosumab in patients with cancer—a surgical strike against the osteoclast. *Nat Rev Clin Oncol* 2012;9:110–8.
- Bilezikian J, Raisz L, Martin T. Principles of Bone Biology: Academic Press; 2008.
- Bussard KM, Gay CV, Mastro AM. The bone microenvironment in metastasis; what is special about bone? *Cancer Metastasis Rev* 2008;27:41–55.
- Lynch CC. Matrix metalloproteinases as master regulators of the vicious cycle of bone metastasis. *Bone* 2010;48:44–53.
- Swanson KR, Rostomily RC, Alvord EC Jr. A mathematical modelling tool for predicting survival of individual patients following resection of glioblastoma: a proof of principle. *Br J Cancer* 2008;98:113–9.
- Anderson AR, Quaranta V. Integrative mathematical oncology. *Nat Rev Cancer* 2008;8:227–34.
- Basanta D, Strand DW, Lukner RB, Franco OE, Cliffler DE, Ayala GE, et al. The role of transforming growth factor-beta-mediated tumor-stroma interactions in prostate cancer progression: an integrative approach. *Cancer Res* 2009;69:7111–20.
- Anderson ARA. A hybrid mathematical model of solid tumour invasion: the importance of cell adhesion. *Math Med Biol* 2005;22:163–86.

10. Pfeilschifter J, Diel I, Scheppach B, Bretz A, Krempien R, Erdmann J, et al. Concentration of transforming growth factor beta in human bone tissue: relationship to age, menopause, bone turnover, and bone volume. *J Bone Miner Res* 1998;13:716–30.
11. Martin T, Gooi JH, Sims NA. Molecular mechanisms in coupling of bone formation to resorption. *Crit Rev Eukaryot Gene Expr* 2009;19:73–88.
12. Chen D, Zhao M, Mundy GR. Bone morphogenetic proteins 1. *Growth Factors* 2004;22:233–41.
13. Kong YY, Yoshida H, Sarosi I, Tan HL, Timms E, Capparelli C, et al. OPGL is a key regulator of osteoclastogenesis, lymphocyte development and lymph-node organogenesis. *Nature* 1999;397:315–23.
14. Mundy GR. Metastasis to bone: causes, consequences and therapeutic opportunities. *Nat Rev Cancer* 2002;2:584–93.
15. Quinn JM, Itoh K, Udagawa N, Hausler K, Yasuda H, Shima N, et al. Transforming growth factor beta affects osteoclast differentiation via direct and indirect actions. *J Bone Miner Res* 2001;16:1787–94.
16. Yasui T, Kadono Y, Nakamura M, Oshima Y, Matsumoto T, Masuda H, et al. Regulation of RANKL-induced osteoclastogenesis by TGF-beta through molecular interaction between Smad3 and Traf6. *J Bone Miner Res* 2011;26:1447–56.
17. Yoneda T, Sasaki A, Mundy GR. Osteolytic bone metastasis in breast cancer. *Breast Cancer Res Treat* 1994;32:73–84.
18. Futakuchi M, Nannuru KC, Varney ML, Sadanandam A, Nakao K, Asai K, et al. Transforming growth factor-beta signaling at the tumor-bone interface promotes mammary tumor growth and osteoclast activation. *Cancer Sci* 2009;100:71–81.
19. Thiollay S, Edwards JR, Fingleton B, Rifkin DB, Matrisian LM, Lynch CC. An osteoblast-derived proteinase controls tumor cell survival via TGF-beta activation in the bone microenvironment. *PLoS ONE* 2012;7:e29862.
20. Shinkai Y, Rathbun G, Lam KP, Oltz EM, Stewart V, Mendelsohn M, et al. RAG-2-deficient mice lack mature lymphocytes owing to inability to initiate V(D)J rearrangement. *Cell* 1992;68:855.
21. Thiollay S, Halpern J, Holt GE, Schwartz HS, Mundy GR, Matrisian LM, et al. Osteoclast-derived matrix metalloproteinase-7, but not matrix metalloproteinase-9, contributes to tumor-induced osteolysis. *Cancer Res* 2009;69:6747–55.
22. Schneider A, Kalikin LM, Mattos AC, Keller ET, Allen MJ, Pienta KJ, et al. Bone turnover mediates preferential localization of prostate cancer in the skeleton. *Endocrinology* 2005;146:1727–36.
23. Coleman RE. Clinical features of metastatic bone disease and risk of skeletal morbidity. *Clin Cancer Res* 2006;12:6243s–9s.
24. Brown JE, Cook RJ, Major P, Lipton A, Saad F, Smith M, et al. Bone turnover markers as predictors of skeletal complications in prostate cancer, lung cancer, and other solid tumors. *J Natl Cancer Inst* 2005;97:59–69.
25. Bonewald LF, Mundy GR. Role of transforming growth factor-beta in bone remodeling. *Clin Orthop Relat Res* 1990;261–76.
26. Rucci N, Teti A. Osteomimicry: how tumor cells try to deceive the bone. *Front Biosci* 2010;2:907–15.
27. Johnson LC, Johnson RW, Munoz SA, Mundy GR, Peterson TE, Sterling JA. Longitudinal live animal micro-CT allows for quantitative analysis of tumor-induced bone destruction. *Bone* 2011;48:141–51.
28. Lipton A, Fizazi K, Stopeck AT, Henry DH, Brown JE, Yardley DA, et al. Superiority of denosumab to zoledronic acid for prevention of skeletal-related events: a combined analysis of 3 pivotal, randomised, phase 3 trials. *Eur J Cancer* 2012;48:3082–92.
29. Lipton A, Steger GG, Figueroa J, Alvarado C, Solal-Celigny P, Body JJ, et al. Randomized active-controlled phase II study of denosumab efficacy and safety in patients with breast cancer-related bone metastases. *J Clin Oncol* 2007;25:4431–7.
30. Horn M, Glauche I, Muller MC, Hehlmann R, Hochhaus A, Loeffler M, et al. Model-based decision rules reduce the risk of molecular relapse after cessation of tyrosine kinase inhibitor therapy in chronic myeloid leukemia. *Blood* 2013;121:378–84.
31. Wilkinson RD. Approximate Bayesian computation (ABC) gives exact results under the assumption of model error. *Stat Appl Genet Mol Biol* 2013;12:129–41.
32. Michor F, Hughes TP, Iwasa Y, Branford S, Shah NP, Sawyers CL, et al. Dynamics of chronic myeloid leukaemia. *Nature* 2005;435:1267–70.
33. Murakami Y, Takada S. Bayesian parameter inference by Markov chain Monte Carlo with hybrid fitness measures: theory and test in apoptosis signal transduction network. *PLoS ONE* 2013;8:e74178.
34. Jayakumar P, Di Silvio L. Osteoblasts in bone tissue engineering. *Proc Inst Mech Eng H* 2010;224:1415–40.
35. Roodman GD. Osteoclast differentiation. *Crit Rev Oral Biol Med* 1991;2:389–409.
36. Ferrier J, Xia SL, Lagan E, Aubin JE, Heersche JN. Displacement and translocation of osteoblast-like cells by osteoclasts. *J Bone Miner Res* 1994;9:1397–405.
37. Dacquin R, Domengot C, Kumanogoh A, Kikutani H, Jurdic P, Machuca-Gayet I. Control of bone resorption by semaphorin 4D is dependent on ovarian function. *PLoS ONE* 2011;6:e26627.
38. Monchau F, Lefevre A, Descamps M, Belquin-myrdycz A, Laffargue P, Hildebrand HF. *In vitro* studies of human and rat osteoclast activity on hydroxyapatite, beta-tricalcium phosphate, calcium carbonate. *Biomol Eng* 2002;19:143–52.
39. Shin H, Zygourakis K, Farach-Carson MC, Yaszemski MJ, Mikos AG. Attachment, proliferation, and migration of marrow stromal osteoblasts cultured on biomimetic hydrogels modified with an osteopontin-derived peptide. *Biomaterials* 2004;25:895–906.
40. UBC. Diffusion rates for molecules Available from: <http://www.math.ubc.ca/~ais/website/status/diffuse.html>
41. Christley S, Alber MS, Newman SA. Patterns of mesenchymal condensation in a multiscale, discrete stochastic model. *PLoS Comput Biol* 2007;3:e76.
42. Kaminska B, Wesolowska A, Danilkiewicz M. TGF beta signalling and its role in tumour pathogenesis. *Acta Biochim Pol* 2005;52:329–37.
43. Wakefield LM, Winokur TS, Hollands RS, Christopherson K, Levinson AD, Sporn MB. Recombinant latent transforming growth factor beta 1 has a longer plasma half-life in rats than active transforming growth factor beta 1, and a different tissue distribution. *J Clin Invest* 1990;86:1976–84.
44. Wergedal J, Stauffer M, Baylink D, Rich C. Inhibition of bone matrix formation, mineralization, and resorption in thyroparathyroidectomized rats. *J Clin Invest* 1973;52:1052–8.
45. Kanehisa J, Heersche JN. Osteoclastic bone resorption: *in vitro* analysis of the rate of resorption and migration of individual osteoclasts. *Bone* 1988;9:73–9.
46. Bloebaum RD, Bachus KN, Momberger NG, Hofmann AA. Mineral apposition rates of human cancellous bone at the interface of porous coated implants. *J Biomed Mater Res* 1994;28:537–44.